



PAPER

Optimizing Dirac fermions quasi-confinement by potential smoothness engineering

RECEIVED
21 November 2019REVISED
22 January 2020ACCEPTED FOR PUBLICATION
6 February 2020PUBLISHED
3 March 2020B Brun¹, N Moreau¹, S Somanchi², V-H Nguyen¹, A Mreńca-Kolasińska³, K Watanabe⁴, T Taniguchi⁴, J-C Charlier¹, C Stampfer² and B Hackens¹¹ IMCN/NAPS & MODL, Université catholique de Louvain (UCLouvain), B-1348 Louvain-la-Neuve, Belgium² JARA-FIT and 2nd Institute of Physics, RWTH Aachen University, 52056 Aachen, Germany³ AGH University of Science and Technology, Faculty of Physics and Applied Computer Science, al. Mickiewicza 30, 30-059 Kraków, Poland⁴ National Institute for Materials Science, Namiki, Tsukuba, JapanE-mail: boris.brun@uclouvain.be and benoit.hackens@uclouvain.be**Keywords:** graphene, Dirac fermions optics, scanning gate microscopySupplementary material for this article is available [online](#)**Abstract**

With the advent of high mobility encapsulated graphene devices, new electronic components ruled by Dirac fermions optics have been envisioned and realized. The main building blocks of electron-optics devices are gate-defined p–n junctions, which guide, transmit and refract graphene charge carriers, just like prisms and lenses in optics. The reflection and transmission are governed by the p–n junction smoothness, a parameter difficult to tune in conventional devices. Here we create p–n junctions in graphene, using the polarized tip of a scanning gate microscope, yielding Fabry–Pérot interference fringes in the device resistance. We control the p–n junctions smoothness using the tip-to-graphene distance, and show increased interference contrast using smoother potential barriers. Extensive tight-binding simulations reveal that smooth potential barriers induce a pronounced quasi-confinement of Dirac fermions below the tip, yielding enhanced interference contrast. On the opposite, sharp barriers are excellent Dirac fermions transmitters and lead to poorly contrasted interferences. Our work emphasizes the importance of junction smoothness for relativistic electron optics devices engineering.

In semiconductor technology, the charge carriers density profile governs the devices' properties. The so-called space charge zone is of fundamental importance in diodes, transistors or solar cells, and its control at the microscopic scale is a prerequisite to reach the desired properties. In graphene, a semi-metal hosting massless Dirac fermions [1], the density profile of a p–n junction plays a really peculiar role. Provided that electronic transport is ballistic, the ratio between the junction width and the Fermi wavelength governs the transmission and refraction properties of charge carriers. In particular, the relativistic Dirac fermions experience Klein tunneling when impinging perpendicularly on a p–n interface [2], which ensures them a perfect unitary transmission independent of the potential barrier height [3]. Additionally, a diverging flow of Dirac fermions is refocused at a p–n interface, similarly to photons entering a negative refraction

index medium [4, 5], an effect denoted as Veselago lensing [6].

These exotic properties of graphene Dirac fermions led to a plethora of electron-optics proposals and realizations, such as electronic optical fibers [7–10], lenses [11–17] and their advanced design to create highly focused electron beams [18], and even the combination of different optical elements to create a scanning Dirac fermions microscope [19]. Aside guiding, the partial reflection encountered at p–n interfaces has been proposed in the early days of graphene to create Fabry–Pérot interferometers with graphene n–p–n junctions [20]. These interferences have since then been observed in monolayer [21–27] as well as multilayer graphene [28, 29]. In view of potential applications, complex n–p–n junction geometries that fully take advantage of these Fabry–Pérot interferences have already proven useful to build otherwise inaccessible

graphene devices, such as reflectors [30, 31] and even transistors [32].

A Fabry–Pérot interferometer consists in two mirrors facing each other, and the transmission probabilities of these mirrors govern the interference fringes contrast. In graphene, the mirrors are materialized by two p–n junctions, and their transmission properties could in principle be tuned by controlling the p–n junctions width. However, p–n junctions in graphene are most often created by means of metallic or graphite gates, whose distance to the graphene plane is by essence fixed, so that the p–n junction width is fixed by the sample geometry. Here we use the polarized tip of a Scanning Gate Microscope (SGM) to induce a n–p–n junction, and take advantage of the SGM flexibility to control and characterize the p–n junctions width, independently of the potential barriers height.

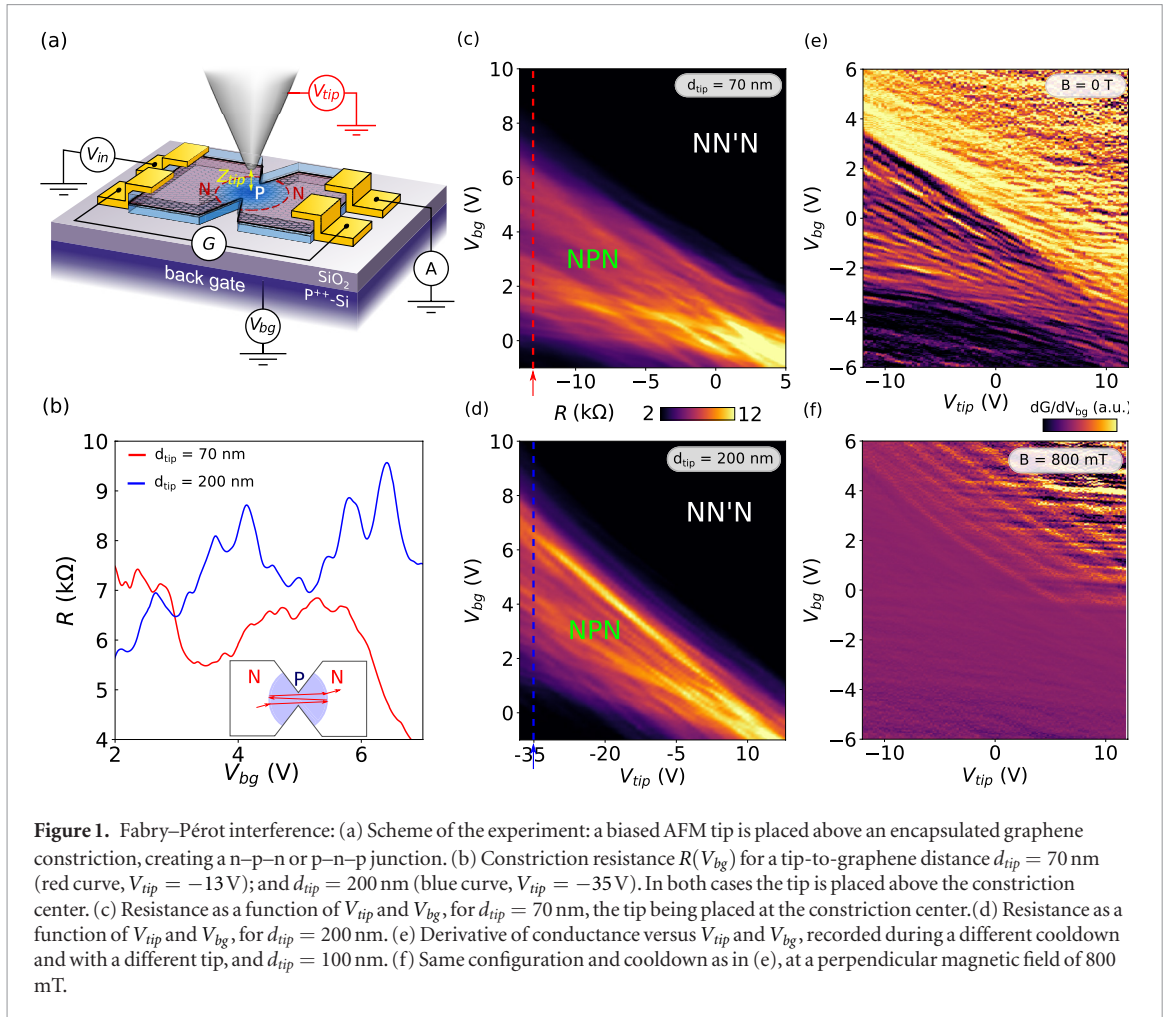
Scanning gate microscopy (SGM) consists in scanning an electrically polarized metallic tip, acting as a local gate above a device’s surface, and mapping out tip-induced device’s conductance changes [33]. Initially developed to investigate transport in III–V semiconductor heterostructures [34–37], SGM brought spatially-resolved insights into transport phenomena occurring in graphene devices, through experiments, simulations and their combination [38–48]. Recently, we demonstrated the viability of SGM to study ballistic transport in clean encapsulated graphene devices, and reported optical-like behavior of Dirac fermions using the tip-induced potential as a Veselago lens [49].

In the present paper, we show that the transmission probabilities of the p–n junctions can be controlled by tuning the SGM tip-to-sample distance. Analyzing our experimental findings in the light of tight-binding simulations, we show that the interferences contrast results from the Dirac fermions confinement efficiency, which is governed by the smoothness of the p–n interfaces.

The studied sample is based on graphene encapsulated between two 20 nm-thick hBN layers, in which a 250 nm-wide constriction is defined by etching [50]. The hBN/graphene/hBN stack lies on top of a highly doped Si substrate covered by a 300 nm SiO₂ insulating layer. This device is thermally anchored to the mixing chamber of a dilution refrigerator, in front of a cryogenic scanning probe microscope [51]. The device conductance G , or resistance R , is measured in 4-contacts configuration, by driving a 1 nA current at a frequency of 77,7 Hz, and recording the voltage between two opposite contacts using standard lock-in technique (as sketched in figure 1(a)). All the data presented here are recorded at a temperature of 100 mK, but global features were found almost independent of temperature up to 1 K, and even a temperature of 4 K did not noticeably change the observed behavior. Most of the data presented here were recorded during a single cooldown (except figures 1(e) and (f)), but this sample showed qualitatively similar behavior for 7 cooldowns.

The biased SGM tip locally changes the carrier density n , leading to a Lorentzian evolution of n , centered at the tip position. When placing the tip at the center of the constriction, a n–p–n or p–n–p configuration can be reached, depending on the tip voltage V_{tip} and back-gate voltage V_{bg} . This is illustrated in figure 1(c) showing resistance as a function of V_{bg} and V_{tip} for a tip-to-graphene distance $d_{tip} = 70$ nm. The n–p–n region, located at the lower left part of figure 1(c), is decorated with a complex pattern of interleaved fringes, resulting from different types of interference phenomena. In the investigated geometry, one can indeed anticipate that, beside the tip-induced n–p–n or p–n–p junction, other confinements play a role and contribute to interferences in the map shown in figure 1(c), such as the constriction defined by etching. Fortunately, increasing the tip-graphene distance to $d_{tip} = 200$ nm yields a clearer picture, shown in figure 1(d), with a much simpler fringe pattern (most of them essentially parallel to the n–p–n/n’-n’-n limit). The visibility of the pattern is also enhanced by their stronger contrast, when compared to the pattern in figure 1(c). In figure 1(b), we plot two profiles of resistance versus V_{bg} , for $d_{tip} = 70$ nm (red curve) and $d_{tip} = 200$ nm (blue curve) where V_{tip} is adapted to reach comparable tip-induced density change (respectively -13 V and -35 V). From this figure, the contrast of the oscillations appears clearly higher for a larger d_{tip} , and a detailed discussion of the origin of this contrast enhancement is one of the main focus of this paper.

It shall first be clarified that these oscillations correspond indeed to Fabry–Pérot interferences arising inside the tip-induced n–p–n region. Figures 1(e) and (f) (recorded during a different cooldown) illustrate the sensitivity of these interference fringes to a perpendicular magnetic field. Figure 1(e) presents the interference pattern recorded by placing the tip above the constriction center ($d_{tip} = 100$ nm). The map in figure 1(e) displays the derivative of G versus V_{bg} to highlight the interference fringes, that appear similar to the ones observed in figures 1(c) and (d). Figure 1(f) shows that they have completely disappeared at a perpendicular magnetic field of 800 mT. From their characteristic decay field, one can infer that these fringes can be associated with a characteristic length, corresponding to a few hundreds nanometer-long cavity, compatible with the cavity formed in the tip induced n–p–n region, as sketched in the inset of figure 1(b) (see supplementary data for additional data and a more detailed discussion (stacks.iop.org/TDM/7/025037/mmedia)). In addition, an accurate determination of the tip-induced potential and an analytical calculation yielding the expected resonances positions in this potential profile agree well with the observed oscillations evolution, as detailed below. All these considerations provide strong evidence that the oscillations correspond to Fabry–Pérot oscillation in the tip-induced n–p–n region. In the remainder of this paper, we will discuss these interference fringes (figures



1(c)–(e) and show that their visibility depends on the smoothness of the p–n junction, controlled by d_{tip} .

As a first step, one needs to precisely evaluate the tip-induced potential. This is done by scanning the tip along the red dashed line figure 2(c) while varying V_{bg} , at fixed V_{tip} and tip-to-graphene distance d_{tip} (i.e. the same procedure described in [49]). The resulting conductance map shown in figure 2(a) exhibits a resistance maximum that follows a Lorentzian shape, as the tip crosses the center of the constriction. This shape is directly related to the shape of the tip-induced potential, as it corresponds to the tip-induced change in the energy of the charge neutrality point at the location of the constriction, which governs the device resistance. Repeating this experiment for several values of d_{tip} , and adapting V_{tip} to keep a constant maximum density change below the tip Δn^{max} , we can fit the different density profiles under the tip influence, provided that the V_{bg} -axis is properly scaled to a density using the backgate lever-arm parameter (see supplementary data).

Considering the tip as a point charge, the expected tip-induced density change would write: $\Delta n(x) = \Delta n^{max}/(1 + x^2/Z_{tip}^2)$, where x is the horizontal distance to the tip center, and Z_{tip} is the effective tip-to-graphene distance, i.e. $Z_{tip} = d_{tip} + a$, a being the tip radius ($a = 50$ nm). We define R_{tip} as

the half-width at half-maximum (HWHM) of this density profile, that is in this expression given by the effective tip height Z_{tip} . Note that this textbook model underestimates the long-range tail of the tip-induced density change (see supplementary data). Accurately modeling the tip-induced potential yields a complex electrostatic problem [52–54], which is beyond the scope of the present paper. In turn, we model Δn with the following phenomenological equation: $\Delta n(x) = \Delta n^{max}/(\sqrt{1 + 3x^2/Z_{tip}^2})$, where we assume that the HWHM R_{tip} is given by Z_{tip} and is therefore known in the experiment, the only free parameter being Δn^{max} . Figure 2(b) shows estimates of tip-induced density changes, for different couples of V_{tip} and d_{tip} leading to the same Δn^{max} (see supplementary data and movie for details).

To study the influence of this potential extension on the Fabry-Pérot oscillations, we place the polarized tip on top of the constriction center (point C in figure 2(c)), and record the resistance as a function of V_{bg} , for different tip-to-graphene distance d_{tip} . As d_{tip} is increased, we decrease V_{tip} (towards more negative values) to keep a constant value of Δn^{max} , and vary only the smoothness of the p–n junctions through R_{tip} . The resulting resistance map is plotted in figure 2(d) and constitutes the main result of this study, together with its detailed theoretical analysis. Figures 2(e) and

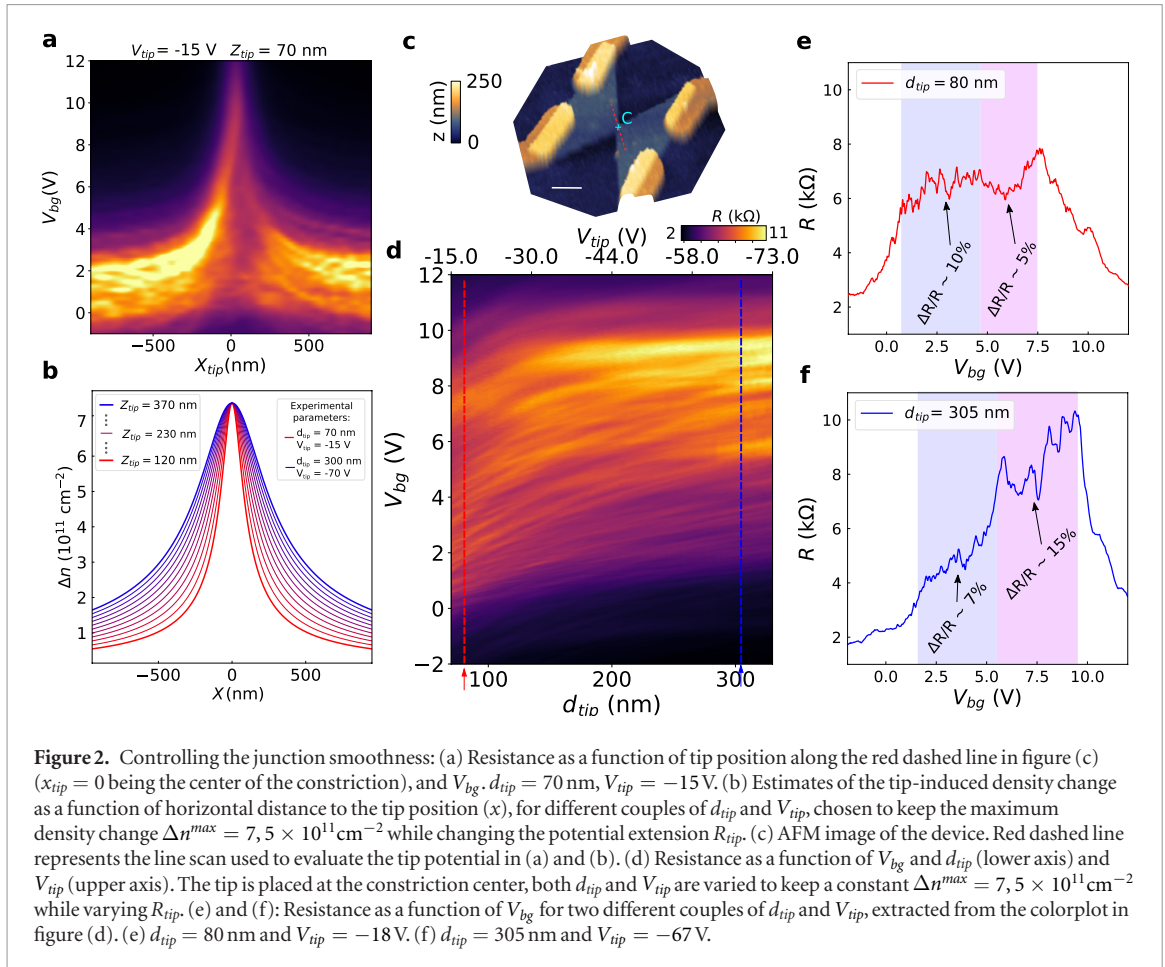


Figure 2. Controlling the junction smoothness: (a) Resistance as a function of tip position along the red dashed line in figure (c) ($x_{tip} = 0$ being the center of the constriction), and $V_{bg} \cdot d_{tip} = 70$ nm, $V_{tip} = -15$ V. (b) Estimates of the tip-induced density change as a function of horizontal distance to the tip position (x), for different couples of d_{tip} and V_{tip} , chosen to keep the maximum density change $\Delta n^{max} = 7,5 \times 10^{11} \text{ cm}^{-2}$ while changing the potential extension R_{tip} . (c) AFM image of the device. Red dashed line represents the line scan used to evaluate the tip potential in (a) and (b). (d) Resistance as a function of V_{bg} and d_{tip} (lower axis) and V_{tip} (upper axis). The tip is placed at the constriction center, both d_{tip} and V_{tip} are varied to keep a constant $\Delta n^{max} = 7,5 \times 10^{11} \text{ cm}^{-2}$ while varying R_{tip} . (e) and (f): Resistance as a function of V_{bg} for two different couples of d_{tip} and V_{tip} , extracted from the colorplot in figure (d). (e) $d_{tip} = 80$ nm and $V_{tip} = -18$ V. (f) $d_{tip} = 305$ nm and $V_{tip} = -67$ V.

(f) show the device resistance as a function of V_{bg} , for two extreme values of R_{tip} in figure 2(d). These two plots highlight two main features already visible in figure 2(d), i.e.:

- (i) The maximum value of the resistance increases with increasing R_{tip} as well as the density for which this maximum is reached.
- (ii) The contrast of the Fabry–Pérot interference evolves in a different way for the lower energy modes observed at low V_{bg} (they decrease in amplitude) and the higher energy ones, whose amplitude increases with R_{tip} .

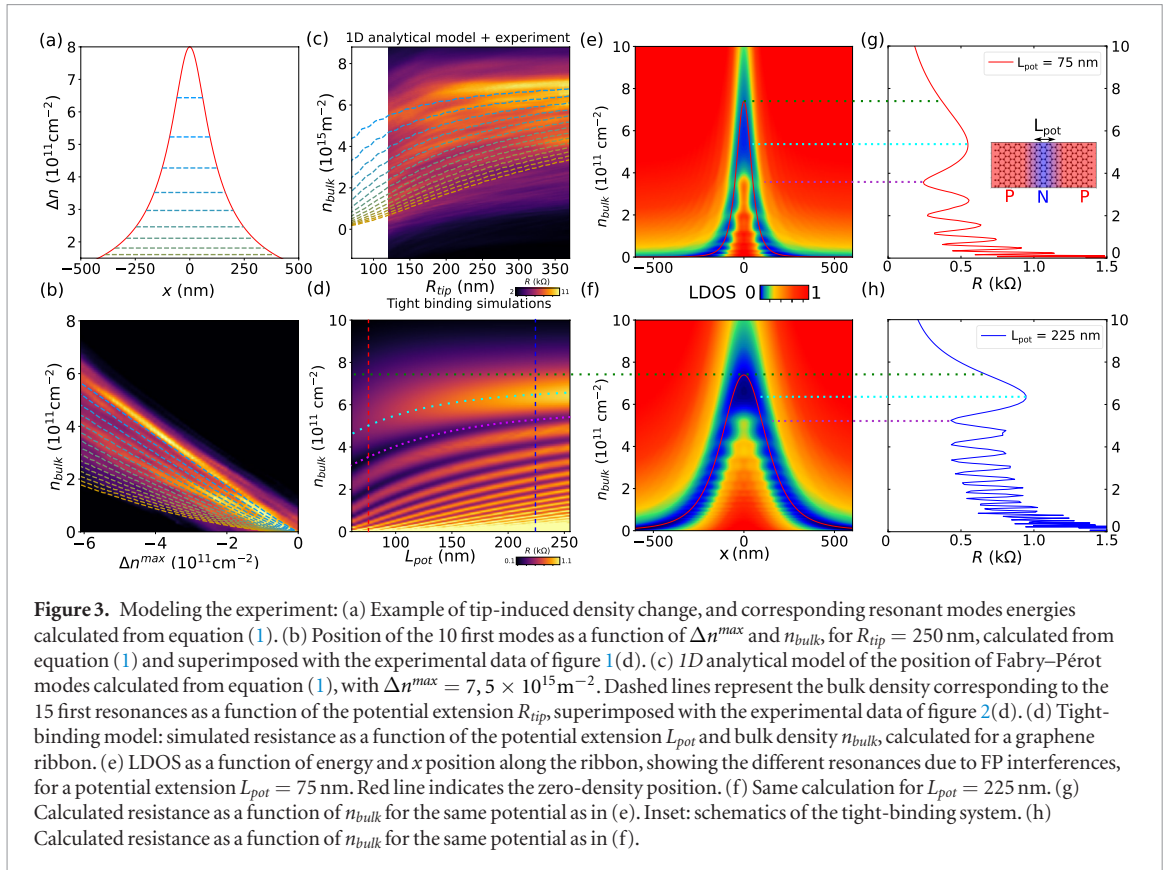
In order to understand these observations, we analyze the problem with two different approaches. The first one is analytic: we use the potential landscape evaluated from figures 2(a) and (b), and follow the approach proposed in [55]. We consider the tip potential as varying only along x -axis, and evaluate the position of the expected resonances from the simple equal phase condition:

$$2 \int_{-L_p}^{L_p} k(x) dx = 2p\pi \quad (1)$$

where L_p is the position of zero charge density along x -axis which depends on the bulk density n_{bulk} , p is a positive integer, and $k(x)$ is the position-dependent

wave-vector evaluated from $n(x)$ provided that $k(x) = \sqrt{\pi n(x)}$. Figure 3(a) shows a typical tip-induced density change and the position of the first resonant modes. In figure 3(b), we calculate the expected position of the 10 first resonant modes for a tip potential extension of 250 nm as a function of n_{bulk} and Δn^{max} , and report them as dashed lines on top of the experimental data of figure 1(d) (where we have used the backgate and tip lever-arm parameters to convert the V_{tip} and V_{bg} axis into carrier densities). There is a good qualitative correspondence between the evolution of the different modes and the experimental fringes, reinforcing the interpretation of their origin as Fabry–Pérot resonances inside the tip-induced n–p–n region. Using $n(x)$ measured for the different couples of d_{tip} and V_{tip} , displayed in figure 2(b), we also plot in figure 3(c) the evolution of the first 15 modes in the (n_{bulk}, R_{tip}) plane, and find that they fall nicely on top of the experimental data of figure 2(d), rescaling the vertical axis V_{bg} to a density and the horizontal axes d_{tip} and V_{tip} to the tip potential extension R_{tip} .

To go one step further in the understanding of the experimental fringes, we perform tight-binding simulations, using a home-made recursive Green functions code [56]. We study a simple graphene ribbon, to which we apply a potential of variable extension L_{pot} along transport direction, (see inset of figure 3(g)), with a smoothness governed by the exponent σ :

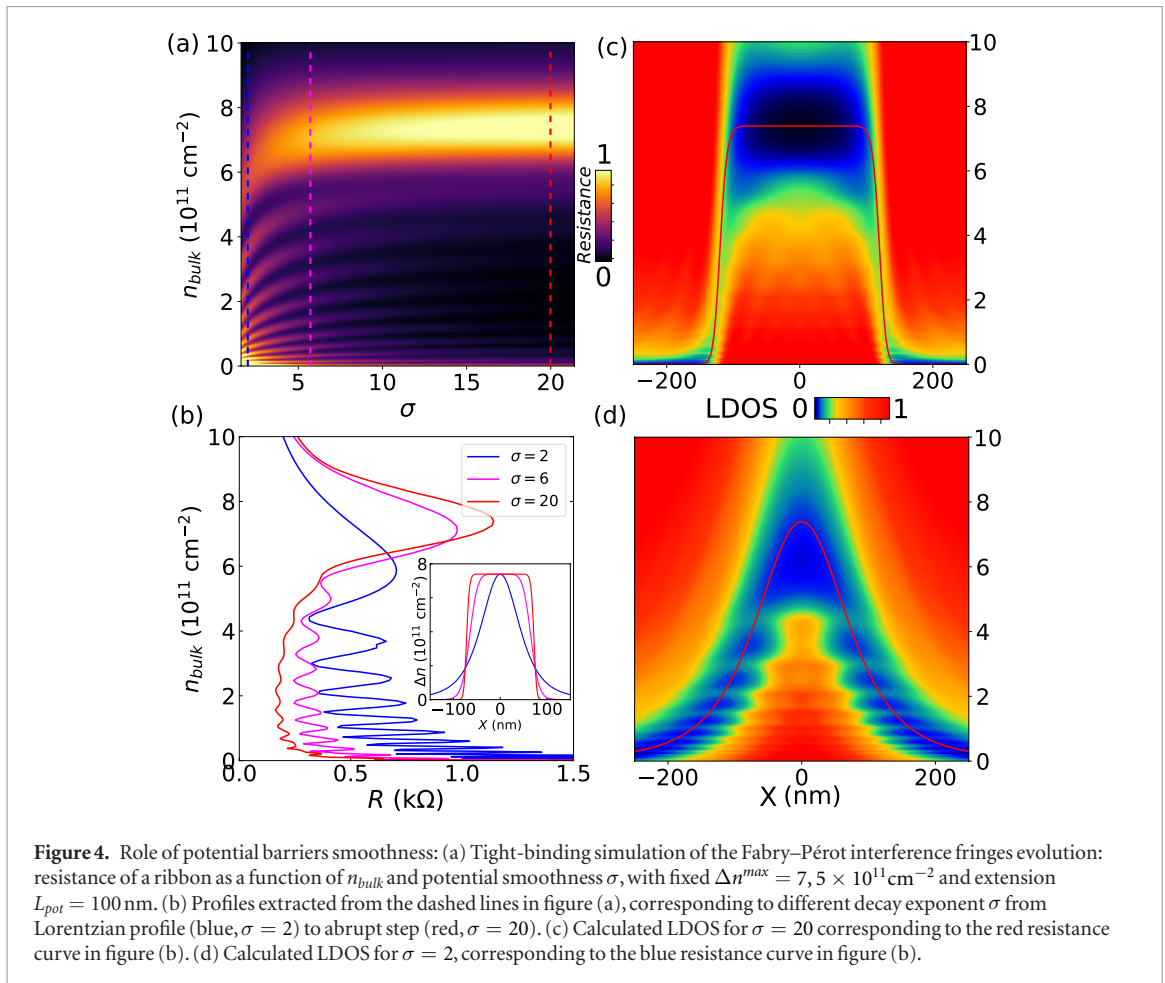


$$V(x) = \frac{V_{max}}{1 + (x/L_{pot})^\sigma}. \quad (2)$$

The ribbon width is fixed to 800 nm to avoid undesirable effects of transverse quantization (Fabry–Pérot resonances are insensitive to the ribbon width). We first consider a Lorentzian potential with $\sigma = 2$, and calculate the ribbon resistance as a function of bulk density n_{bulk} (i.e. the charge carrier density in the p region) and potential extension L_{pot} , while keeping a fixed value of $\Delta n^{max} = 7,5 \times 10^{11} \text{ cm}^{-2}$. The result is plotted in figure 3(d). First of all, the average resistance increases with the tip potential extension, which appears consistent with the experiment. This fact can be explained by Klein tunneling, which becomes less efficient and more angle selective with smoother junctions. It shall also be noted that the first resistance maximum (cyan dotted line on figure 3(d)) is not obtained for $n_{bulk} = -\Delta n^{max}$ (green dotted line). This is clarified in figure 3(e), where we plot the local density of states (LDOS) in the graphene ribbon integrated over the transverse direction, as a function of n_{bulk} , aside with the resistance as a function of bulk density (figure 3(g)), for a potential extension $L_{pot} = 75$ nm. There is indeed a clear offset between the bulk density corresponding to the maximum of the tip-induced potential in figure 3(e) (indicated by a green dotted line) and the resistance maximum in figure 3(g) (indicated by a cyan dotted line). The resistance maximum is rather reached for a density n_{bulk} yielding a minimum LDOS at the barrier center.

Figures 3(f) and (h) present the same analysis for a larger potential extension. In this case, the bulk densities corresponding to Δn^{max} (in green) and to the minimum LDOS (in cyan) are closer to each other, but still do not match. The respective evolution of these two densities with the potential extension can be followed figure 3(d), as the spacing between the green and cyan dotted lines, and is in good agreement with the evolution of the resistance maximum observed in the experiment, as visible in figures 2(d) and (c).

A second interesting feature well captured by this toy model is the evolution of the first resonant mode energy, visible as the first resistance minimum indicated by purple dashed lines in figures 3(e)–(h), which follows roughly the same average evolution as the resistance maximum. This first Fabry–Pérot mode energy is reminiscent of the confinement energy due to the potential well created by the tip. In quantum mechanics, a famous textbook problem consists in finding the zero-point energy of a ‘particle-in-a-box’, i.e. trapped in an infinite square potential of length L . The zero-point energy in the latter case emerges as a consequence of Heisenberg uncertainty principle, and increases with decreasing L (as L^{-2} for massive particles and L^{-1} for massless Dirac fermions [57]). This distance of the first mode to the maximum of the tip potential is also clearly dependent on R_{tip} in the experiment, as visible in figures 2(d) and (c). It provides a nice illustration of this textbook problem, poorly explored in the case of Dirac fermions due to the inherent difficulty to confine them.



Discrepancies are however visible between results from this ideal ribbon model and experimental data. First of all, additional resonances are present in the experiment. They could result from the transverse quantization inherent to the narrow constriction, intentionally suppressed in the tight-binding model by simulating a wide ribbon. These additional resonances could also arise from disorder, and the finite distance between the contacts and the constriction, that could lead to other Fabry–Pérot cavities. Secondly, the high resistance at low bulk density in the model is not present in the experiment. This can easily be understood as due to the experimentally measured finite resistance at the Dirac point, inherent to residual electron-hole puddles at low densities, whereas the tight-binding calculation in a homogeneous graphene ribbon predicts a much larger resistance of the bulk (and leads) close to the Dirac point. Both effects prevent the direct quantitative comparison of the interferences contrast in the experiment and the model presented in figure 3.

To better understand the influence of the tip potential extension, we perform additional tight-binding simulations and vary the potential steepness by changing the decay exponent σ in equation (2). We first calculate the resistance of the ribbon as a function of bulk density and decay exponent, and plot the result in figure 4(a). For three different decay exponents ($\sigma = 2, 6, 20$) we extract the resistance as a function of n_{bulk} and plot the result in figure 4(b). These two

figures evidence that the potential smoothness is a key ingredient, that governs the Fabry–Pérot interference contrast. Indeed, the relativistic nature of graphene charge carriers makes sharp potential barriers highly transparent due to Klein tunneling. As a consequence, the Fabry–Pérot resonances in the LDOS are rather large and overlap (see figure 4(c)), owing to their hybridization with the Dirac continuum of the bulk. This weak confinement yields poorly contrasted Fabry–Pérot oscillations in the total resistance (red curve figure 4(b)). In contrast, a smooth p–n junction (on the Fermi wavelength scale) is a poor Dirac fermions transmitter, so that two facing smooth p–n junctions can be used to confine Dirac fermions in a more efficient way. This can be seen figure 4(d), where the LDOS in the case of a smooth n–p–n junction is plotted, and exhibits well defined resonant modes, giving rise to pronounced Fabry–Pérot oscillations in the resistance (blue curve figure 4(b)).

The confinement of Dirac fermions in p–n nanoislands and the resulting LDOS resonances have recently been explored in a set of beautiful scanning tunneling microscopy experiments [58–61]. In this SGM experiment, with a fixed tip at the center of the constriction, we cannot reveal the rich internal LDOS structure of the tip-induced circular p–n island, including e.g. whispering gallery modes [59]. However, it allows to probe transport through such an island and reveals the strength of LDOS resonances

through Fabry–Pérot oscillations in the device resistance. Tight-binding simulations explicitly confirm that the interference contrast is related to the LDOS resonances strength, themselves governed by the p–n junction smoothness, which can be easily tuned in SGM, as demonstrated here.


In conclusion, we defined a n–p–n junction in a high mobility graphene sample using the polarized tip of a scanning gate microscope. Oscillating patterns are observed in transport through the n–p–n junction that can be attributed to Fabry–Pérot interferences. By simultaneously varying the tip-to-graphene distance and tip voltage, one can control and characterize the p–n junctions smoothness. In turn, this allowed to show that smoother p–n junctions induce a larger contrast of the interference fringes. Using tight-binding simulations, we studied the influence of the p–n junctions smoothness on the LDOS resonances, resulting from the quasi-confinement of Dirac fermions within the tip-induced potential. These LDOS resonances amplitude can be explicitly linked to the visibility of the Fabry–Pérot oscillations. In the quest towards ever reduced graphene devices size, gates are often placed as close as possible to the graphene plane. The present study recalls that the gate dielectric thickness governs the p–n junction smoothness, which strongly influences the visibility of interferences. It then governs the efficiency of devices based on electron-optics concepts. This underlines that these distances have to be cleverly adjusted in the conception of relativistic electron optics devices.

Acknowledgments

The present research was funded by the Fédération Wallonie–Bruxelles through the ARC Grant on 3D nanoarchitecturing of 2D crystals (No. 16/21-077) and from the European Union’s Horizon 2020 Research and Innovation program (No. 696656). B B (research assistant), N M (FRIA fellowship), B H (research associate), V-H N and J-C C (PDR No. T.1077.15 and ERA-Net No. R.50.07.18.F and CDR project No. J008019F) acknowledge financial support from the F R S-FNRS of Belgium. Support by the Helmholtz Nanoelectronic Facility (HNF), the EU ITN SPINOGRAPH and the DFG (SPP-1459) is gratefully acknowledged. Growth of hexagonal boron nitride crystals was supported by the Elemental Strategy Initiative conducted by the MEXT, Japan and JSPS KAKENHI Grant Numbers JP26248061, JP15K21722 and JP25106006. Computational resources have been provided by the Consortium des équipements de Calcul Intensif (CECI), funded by the Fonds de la Recherche Scientifique de Belgique (FRS-FNRS) under Grant No. 2.5020.11 and by the Walloon Region. B B acknowledges the use of Kwant [62] used to guide the experiment and cross-check tight-binding simulations.

ORCID iDs

B Brun  <https://orcid.org/0000-0001-7403-2484>

V-H Nguyen  <https://orcid.org/0000-0001-6729-3520>

K Watanabe  <https://orcid.org/0000-0003-3701-8119>

References

- [1] Novoselov K S, Geim A K, Morozov S V, Jiang D, Katsnelson M I, Grigorieva I V, Dubonos S V and Firsov A A 2005 *Nature* **438** 197
- [2] Klein O 1929 *Z. Phys.* **53** 157
- [3] Allain P E and Fuchs J N 2011 *Eur. Phys. J. B* **83** 301
- [4] Cheianov V V, Fal’ko V and Altshuler B L 2007 *Science* **315** 1252
- [5] Milovanovi S P, Moldovan D and Peeters F M 2015 *J. Appl. Phys.* **118** 154308
- [6] Veselago V G 1968 *Sov. Phys.–Usp.* **10** 509
- [7] Beenakker C W J, Sepkhanov R A, Akhmerov A R and Tworzydło J 2009 *Phys. Rev. Lett.* **102** 146804
- [8] Hartmann R R, Robinson N J and Portnoi M E 2010 *Phys. Rev. B* **81** 245431
- [9] Williams J R, Low T, Lundstrom M S and Marcus C M 2011 *Nat. Nanotechnol.* **6** 222
- [10] Rickhaus P, Liu M-H, Makk P, Maurand R, Hess S, Zihlmann S, Weiss M, Richter K and Schönenberger C 2015 *Nano Lett.* **15** 5819
- [11] Cserti J, Pályi A and Péterfalvi C 2007 *Phys. Rev. Lett.* **99** 246801
- [12] Mu W, Zhang G, Tang Y, Wang W and Ou-Yang Z 2011 *J. Phys.: Condens. Matter* **23** 495302
- [13] Garg N A, Ghosh S and Sharma M 2014 *J. Phys.: Condens. Matter* **26** 155301
- [14] Wu J-S and Fogler M M 2014 *Phys. Rev. B* **90** 235402
- [15] Logemann R, Reijnders K J A, Tudorovskiy T, Katsnelson M I and Yuan S 2015 *Phys. Rev. B* **91** 045420
- [16] Lu M and Zhang X-X 2018 *J. Phys.: Condens. Matter* **30** 215303
- [17] Zhang S-H, Yang W and Peeters F M 2018 *Phys. Rev. B* **97** 205437
- [18] Liu M-H, Gorini C and Richter K 2017 *Phys. Rev. Lett.* **118** 066801
- [19] Bøggild P, Caridad J M, Stampfer C, Calogero G, Papior N R and Brandbyge M 2017 *Nat. Commun.* **8** 15783
- [20] Shytov A V, Rudner M S and Levitov L S 2008 *Phys. Rev. Lett.* **101** 156804
- [21] Young A F and Kim P 2009 *Nat. Phys.* **5** 222
- [22] Velasco J, Liu G, Bao W and Lau C N 2009 *New J. Phys.* **11** 095008
- [23] Nam S-G, Ki D-K, Park J W, Kim Y, Kim J S and Lee H-J 2011 *Nanotechnology* **22** 415203
- [24] Rickhaus P, Maurand R, Liu M-H, Weiss M, Richter K and Schönenberger C 2013 *Nat. Commun.* **4** 2342
- [25] Oksanen M, Uppstu A, Laitinen A, Cox D J, Craciun M F, Russo S, Harju A and Hakonen P 2014 *Phys. Rev. B* **89** 121414
- [26] Handschin C, Makk P, Rickhaus P, Liu M-H, Watanabe K, Taniguchi T, Richter K and Schönenberger C 2017 *Nano Lett.* **17** 328
- [27] Veyrat L, Jordan A, Zimmermann K, Gay F, Watanabe K, Taniguchi T, Sellier H and Sacépé B 2019 *Nano Lett.* **19** 635
- [28] Varlet A, Liu M-H, Krueckl V, Bischoff D, Simonet P, Watanabe K, Taniguchi T, Richter K, Ensslin K and Ihn T 2014 *Phys. Rev. Lett.* **113** 116601
- [29] Campos L C, Young A F, Surakitbovorn K, Watanabe K, Taniguchi T and Jarillo-Herrero P 2012 *Nat. Commun.* **3** 1239
- [30] Morikawa S, Wilmart Q, Masubuchi S, Watanabe K, Taniguchi T, Plaçais B and Machida T 2017 *Semicond. Sci. Technol.* **32** 045010
- [31] Graef H et al 2019 *Nat. Commun.* **10** 2428

- [32] Wang K, Elahi M M, Wang L, Habib K M M, Taniguchi T, Watanabe K, Hone J, Ghosh A W, Lee G-H and Kim P 2019 *Proc. Natl Acad. Sci.* **116** 6575
- [33] Eriksson M A, Beck R G, Topinka M, Katine J A, Westervelt R M, Campman K L and Gossard A C 1996 *Appl. Phys. Lett.* **69** 671
- [34] Topinka M A, LeRoy B J, Westervelt R M, Shaw S E J, Fleischmann R, Heller E J, Maranowski K D and Gossard A C 2001 *Nature* **410** 183
- [35] Jura M P, Topinka M A, Grobis M, Pfeiffer L N, West K W and Goldhaber-Gordon D 2009 *Phys. Rev. B* **80** 041303
- [36] Kozikov A A, Rössler C, Ihn T, Ensslin K, Reichl C and Wegscheider W 2013 *New J. Phys.* **15** 013056
- [37] Brun B et al 2014 *Nat. Commun.* **5** 4290
- [38] Schnez S, Güttinger J, Huefner M, Stampfer C, Ensslin K and Ihn T 2010 *Phys. Rev. B* **82** 165445
- [39] Pascher N, Bischoff D, Ihn T and Ensslin K 2012 *Appl. Phys. Lett.* **101** 063101
- [40] Garcia A G F, König M, Goldhaber-Gordon D and Todd K 2013 *Phys. Rev. B* **87** 085446
- [41] Cabosart D, Felten A, Reckinger N, Iordanescu A, Toussaint S, Faniel S and Hackens B 2017 *Nano Lett.* **17** 1344
- [42] Bhandari S, Lee G-H, Klaes A, Watanabe K, Taniguchi T, Heller E, Kim P and Westervelt R M 2016 *Nano Lett.* **16** 1690
- [43] Xiang S, Mreńca-Kolasińska A, Miseikis V, Guiducci S, Kolasiński K, Coletti C, Szafran B, Beltram F, Roddaro S and Heun S 2016 *Phys. Rev. B* **94** 155446
- [44] Mreńca-Kolasińska K, Kolasiński A and Szafran B 2015 *Semicond. Sci. Technol.* **30** 085003
- [45] Mreńca-Kolasińska A, Heun S and Szafran B 2016 *Phys. Rev. B* **93** 125411
- [46] Mreńca-Kolasińska A and Szafran B 2017 *Phys. Rev. B* **96** 165310
- [47] Petrović M D, Milovanović S P and Peeters F M 2017 *Nanotechnology* **28** 185202
- [48] Dou Z et al 2018 *Nano Lett.* **18** 2530
- [49] Brun B, Moreau N, Somanchi S, Nguyen V-H, Watanabe K, Taniguchi T, Charlier J-C, Stampfer C and Hackens B 2019 *Phys. Rev. B* **100** 041401
- [50] Terrés B et al 2016 *Nat. Commun.* **7** 11528
- [51] Hackens B, Martins F, Faniel S, Dutu C A, Sellier H, Huant S, Pala M, Desplanque L, Wallart X and Bayot V 2010 *Nat. Commun.* **1** 39
- [52] Zhang L M and Fogler M M 2008 *Phys. Rev. Lett.* **100** 116804
- [53] Żebrowski D, Mreńca-Kolasińska A and Szafran B 2018 *Phys. Rev. B* **98** 155420
- [54] Chaves F A, Jimnez D, Santos J E, Bøggild P and Caridad J M 2019 *Nanoscale* **11** 10273
- [55] Drienovsky M, Schrettenbrunner F-X, Sandner A, Weiss D, Eroms J, Liu M-H, Tkatschenko F and Richter K 2014 *Phys. Rev. B* **89** 115421
- [56] Nguyen V H, Bournel A and Dollfus P 2010 *J. Phys.: Condens. Matter* **22** 115304
- [57] Cho S and Fuhrer M 2011 *Nano Res.* **4** 385
- [58] Gutiérrez C, Brown L, Kim C-J, Park J and Pasupathy A N 2016 *Nat. Phys.* **12** 1069
- [59] Zhao Y, Wyrick J, Natterer F D, Rodriguez-Nieva J F, Lewandowski C, Watanabe K, Taniguchi T, Levitov L S, Zhitenev N B and Strosio J A 2015 *Science* **348** 672
- [60] Lee J et al 2016 *Nat. Phys.* **12** 1032
- [61] Jiang Y, Mao J, Moldovan D, Masir M R, Li G, Watanabe K, Taniguchi T, Peeters F M and Andrei E Y 2017 *Nat. Nanotechnol.* **12** 1045
- [62] Groth C W, Wimmer M, Akhmerov A R and Waintal X 2014 *New J. Phys.* **16** 063065